Adapting confocal Raman microscopy for *in situ* studies of redox transformations at electrode-electrolyte interfaces

by

Carol Korzeniewski[⊥†]*, Eric M. Peterson[†], Jay P. Kitt[†], Shelley D. Minteer[†] and Joel M. Harris[†]*

Abstract. Confocal Raman microscopy was applied to quantify redox species present within the diffusion layer adjacent to an electrode surface under potentiostatic control. A glass microscope coverslip with a thin indium tin oxide (ITO) coating served as both the working electrode and optical window for a microscope-stage mountable spectroelectrochemical cell. A high numerical aperture objective mounted in an inverted microscope frame just below the stage brought excitation radiation through the coverslip window and to a tight focus a few micrometers above the ITO film surface. Species diffusing into the confocal probe volume defined by the excitation beam focus and the collected light region were detected, identified and quantified based on their Raman scattering frequencies and intensities. In measurements that interrogated the interconversion of ferrocyanide and ferricyanide ions as a function of applied voltage, least-squares regression analysis of spectral datasets predicted the formal potential and relative surface concentrations of the ions in good agreement with the expected Nernstian response. Preliminary studies of methyl viologen reduction at an ITO film / Nafion membrane interface were conducted and show the possibility for estimation of mass transport coefficients of redox species within ionic polymer materials.

KEYWORDS: confocal Raman microscopy, spectroelectrochemistry, diffusion layer, mass transport, polymer modified electrode

[⊥] Department of Chemistry and Biochemistry, Texas Tech University, Lubbock, TX 79409-1061

[†] Department of Chemistry, University of Utah, Salt Lake City, UT 84112

* Corresponding authors: carol.korzeniewski@ttu.edu, harrisj@chem.utah.edu

1. Introduction

As strategies for performing in-situ spectroscopic measurements of electrode processes advance, infrared and Raman techniques remain at the forefront as versatile probes of interfacial molecular composition and structure.[1-6] Many applications leverage the innate surface sensitivity of the reflectance infrared and surface-enhanced infrared and Raman spectroscopy to detect adsorbed molecular species and to investigate the effects of adsorbate coverage and orientation on charge transfer processes.[1-4,7,8] In the study of nano- and micron-scale thin films on electrodes, however, these spectroscopic approaches are not as effective. Optical dispersion effects cause spectral band distortions in reflectance measurements, and sensitivity has limited spatial extent as surface enhanced electromagnetic fields decay with distance from the electrode.[5,9-11] In recent years, Raman microscopy sampling has been advanced for probing chemical environment within polymer electrolytes and redox-active thin films in contact with electrodes.[12-18] Operando measurements on low-temperature fuel cells have been demonstrated and factors unique to the spectroelectrochemical platform that affect sensitivity have been evaluated.[12,13,15] More recently, Raman and scanning electrochemical microscopy techniques have been combined to explore structure/reactivity correlations within localized regions of redox-active materials important for energy conversion and storage.[16-18]

The reported work adapts confocal Raman microscopy to detect and quantify species present within the diffusion layer that develops at an electrode in response to changes in applied potential. The confocal Raman optical arrangement aligns the excitation beam focus with an aperture in the image (detection) plane to restrict light from outside the focal volume from reaching the detector.[19,20] The region of the beam focus from which detected scattered light originates is referred to as the confocal probe volume.[20] For a Raman excitation source in the visible or near infrared

frequency region, the confocal probe volume occupies a few femtoliters when the beam is focused to a diffraction-limited spot within a sample.[19,20]

The spectra presented herein were recorded with the confocal probe volume of a Raman microscope positioned within an electrolyte-filled spectroelectrochemical cell and focused a few micrometers from the working electrode surface. The confocal probe volume sampled species present within the diffusion layer adjacent to the electrode. For a reversible redox moiety ($[Fe(CN)_6]^{3-/4-}$) in an aqueous electrolyte solution, the concentrations of the oxidized and reduced forms at the confocal probe volume position were determined from spectra collected as a function of applied potential. Least-squares regression analysis of the spectral datasets predicted the formal potential of the redox couple and the steady-state concentrations of the oxidized and reduced forms at each potential in excellent agreement with the expected Nernstian response. Spectra that track the concentration front of a slowly diffusing redox species electrogenerated within a polymer electrolyte are also presented.

2. Materials and Methods

2.1. Reagents. Aqueous solutions were prepared from 18 MΩ-cm water dispensed from a Barnstead GenPure UV water filtration system. 2-propanol (Optima, ≥ 99%) solvent was from Fischer Scientific (Waltham, MA, USA). Methyl viologen (MV) dichloride (98%) was from Sigma-Aldrich (Saint Louis, MO, USA). Potassium and sodium chloride (Macron Chemicals) and potassium hexacyanoferrate(II) and (III) (Aldrich) were reagent grade or better and used as received. Nafion 112 (50 μm thickness) membrane was from Ion Power (Newcastle, DE, USA). A sample of approximately 5 mm x 5 mm was cut and cleaned by brief boiling in 0.1 M NaCl containing 0.3 % H_2O_2.[20] After rinsing in deionized water, the sample was transferred to boiling

0.1 M NaCl to complete the ion exchange. The sample was rinsed in boiling deionized water to remove excess salt and stored dry until use. Just prior to spectral measurements, the sample was soaked in aqueous 10 mM MV^{2+} for 30 min and subsequently rinsed in deionized water to eliminate excess MV species from the membrane.

2.2. Electrochemical cells. For spectroelectrochemistry, in this work a microscope-stage mountable cell designed for fluorescence microscopy imaging of probe ions at a potential-controlled interface was adapted.[21] The cell was constructed around a glass microscope coverslip containing a sputter-coated indium tin oxide (ITO) film on one side (22 mm x 22 mm, 15-30 Ω/cm, SPi Supplies, West Chester, PA, USA). The ITO-coated coverslip served as both the working electrode and window for coupling light into the cell. Intended for use with an inverted microscope,[21] the coverslip also formed the bottom of the electrolyte-filled reservoir for the cell. A poly-tetrafluoroethylene (PTFE) insert was sealed against the coverslip to form a chamber for the electrolyte solution and the counter and reference electrodes.[16] A gasket at the foot of the PTFE insert pressed a thin metal foil serving as the lead for the working electrode against the ITO-coated surface, while isolating the metal foil from contact with the electrolyte solution. When secured to the microscope stage, the objective contacted the outer (glass) side of the ITO-coated coverslip through a droplet of immersion oil (IMMOIL-F30CC (n = 1.51), Olympus (Waltham, MA, USA)). Prior to cell assembly, the ITO-coated coverslip was cleaned by first rinsing in 2-propanol followed by 18 MΩ-cm water and subsequently treatment in a UV/ozone cleaner.[21] The cell was used with a platinum mesh counter electrode and a saturated calomel electrode (SCE) reference. During spectroelectrochemical measurements, the electrolyte solution was at ambient temperature (21.0 ± 0.5 °C) and exposed to the laboratory atmosphere. Cyclic voltammetry performed with a

platinum working electrode employed a conventional glass cell and platinum mesh counter and SCE reference electrodes.

2.3. Instrumentation. The confocal Raman microscope system is based on a previously reported design.[19,22] The excitation source was a single-mode diode-pumped solid-state laser operating at 660 nm (Gem 660, Laser Quantum, Fremont, CA, USA). The laser beam was expanded (10 ×, Thorlabs, Newton, NJ, USA) and directed toward the rear entrance port of a Nikon Eclipse TE-200 inverted microscope (Nikon, El Segundo, CA, USA), where it was spectrally filtered (Semrock, Lake Forest, IL, USA) and reflected from a dichroic mirror (Semrock) to slightly overfill the rear aperture of a 100×, 1.49 N.A. oil immersion objective (Nikon, CFI Apochromat TIRF). The objective focused the beam into the spectroelectrochemical cell through the ITO-coated glass coverslip. The near diffraction-limited probe volume was positioned ~3 μm above the ITO-electrolyte interface (Scheme 1) using reflection from the ITO-electrolyte interface as a guide to axial positioning.[19,23] Raman scattered light was collected back through the same microscope objective. The radiation passed through the dichroic mirror and a final long-pass filter (Semrock) before being focused onto the entrance slit (50 μm) of a grating monochromator (Shamrock 500i, Andor, Belfast, UK). The diffraction grating, 300 lines/mm blazed at 760 nm, dispersed Raman scattered light from the slit image onto a charge-coupled device (CCD) camera (iDus DU416A, Andor), achieving a limiting resolution of 1.66 cm^{-1}/pixel. To match the spectrograph slit width, every three pixels were binned horizontally, giving a spectral resolution of 5 cm^{-1}. The confocal aperture was defined using the

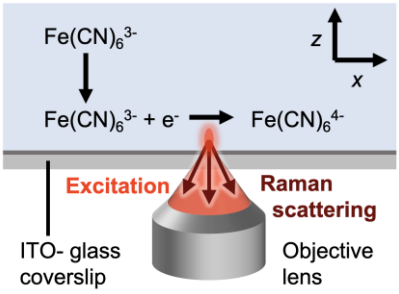

Scheme 1. Depiction of the *in situ* confocal Raman spectro-electrochemical measurement. The inset axes show the axial (z) and in-plane (x) directions. The y direction (not shown) is in-plane and orthogonal to x and z.

entrance slit of the monochromator in the horizontal dimension and by binning five rows of pixels on the CCD camera (75 μm) in the vertical dimension.[19,22,24]

Cyclic voltammograms were recorded using a WaveNow (Pine Research, Durham, NC USA) potentiostat running AfterMath software. A Pine AFCBP1 bipotentiostat was used to control the cell potential during *in situ* confocal Raman microscopy measurements.

2.4. Data Analysis. Spectral data were processed and analyzed on desktop computers using custom scripts executed in Matlab (version R2020b; MathWorks, Natick, MA, USA). After subtraction of a dark current offset, Raman spectra were corrected for instrument response by ratioing to a recorded spectrum of emission from a standard reference halogen source lamp (SL1-CAL, StellarNet, Tampa, FL, USA).[25-27] Spectral baselines were corrected using a rolling-circle[28] high pass filter. Scripts for factor analysis[29] and least-squares regression analysis[30,31] utilized the Matlab *pca* and *fminsearch* functions, respectively. Non-linear least-squares fitting was performed using the Microsoft Excel Solver add-in (Redmond, WA, USA).

3. Results and Discussion

3.1. Ferricyanide reduction. Figure 1 contains cyclic voltammograms recorded with an ITO-coated glass coverslip mounted in the spectroelectrochemical cell and serving as the working electrode. In the absence of a redox probe, only charging current is evident in voltammograms obtained with the ITO surface in contact with clean 0.2 M KCl electrolyte (Figure 1, bottom). Redox waves begin to appear following the addition of ferricyanide to the cell (Figure 1, middle). A cyclic voltammogram recorded using a platinum working electrode is included (Figure 1, top) to show the anticipated response associated with reversible electron transfer. The formal potential estimated from the voltammogram (0.22 V) is in good agreement with earlier reports for

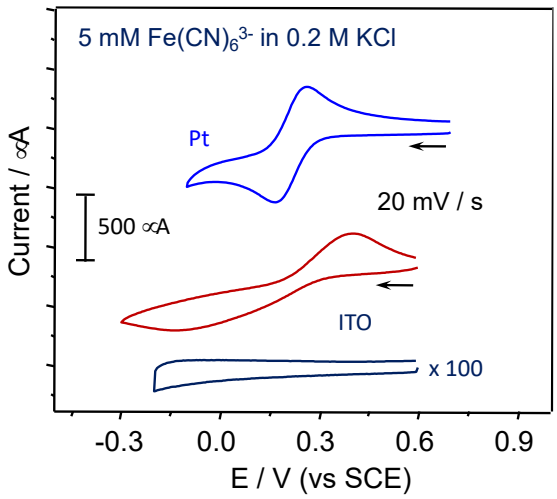

Figure 1. Cyclic voltammograms recorded in 0.2 M KCl with (top and middle) and without (bottom) added 4.0 mM $K_3Fe(CN)_6$. The working electrodes used were a platinum wire (top) and an ITO film coated glass microscope coverslip (middle and bottom). The scan rate was 20 mV/s.

ferricyanide and ferrocyanide species in KCl electrolyte.[32] For the ITO film electrode, the wide separation of cathodic and anodic peaks can be attributed to film resistance and possible effects of limited surface activation. The response becomes more ideal as the scan rate is slowed and, as discussed below, the steady-state concentrations of redox species in the near-surface layer derived from confocal Raman spectra are as expected for a reversible reaction.

Ferricyanide (and ferrocyanide) have often been used to assess the performance of spectroelectrochemical detection strategies.[32-34] In addition to the stability and quasi-reversible response of the redox couple, the complexes have prominent C ≡ N stretching vibrational features that are convenient for evaluating sensitivity in cells designed for coupling to infrared or Raman probes. Figure 2 displays Raman spectra collected with the confocal probe volume positioned in the spectro-electrochemical cell a few micrometers above the ITO film (Scheme 1). As a guide to positioning, the excitation beam was first brought to a sharp focus at the coverslip-solution interface and then raised to a position approximately 3 μm above the ITO film surface, a height that ensures the axial extension of the confocal probe volume at 90 % detection efficiency (*vide infra*) is well beyond the coverslip. When the ITO film is poised at 0.7 V, the experimental spectrum is dominated by a strong band near 2131 cm^{-1} characteristic of the overlapping ν_1 (A_{1g} symmetry) and ν_3 (E_{2g} symmetry) C ≡ N stretching vibrational modes of $Fe(CN)_6^{3-}$ ions.[35,36] As the potential is stepped negative, additional bands begin to appear at 2092

cm^{-1} and 2057 cm^{-1} signaling $Fe(CN)_6^{3-}$ reduction to $Fe(CN)_6^{4-}$ is occurring at the ITO film surface. The 2092 cm^{-1} and 2057 cm^{-1} bands map to the respective ν_1 and ν_3 C ≡ N stretching vibrational modes of $Fe(CN)_6^{4-}$ ions.[35,36] Scheme 1 depicts the confocal Raman microscopy measurement probing the diffusion layer under these conditions of $Fe(CN)_6^{3-}$ transport from bulk solution followed by reduction at the ITO film surface. At 0.2 V, near the formal potential for the ferrocyanide/ferricyanide couple,[32] the experimental spectrum in Figure 2 clearly indicates the two redox species are present at the electrode-solution interface. As the potential is stepped further negative, features of ferrocyanide become dominant. Raman spectra of aqueous solutions containing ferricyanide and ferrocyanide are included in Figure 3 and confirm the spectral bands observed in Figure 2 arise from $Fe(CN)_6^{3-}$ and $Fe(CN)_6^{4-}$ complexes.

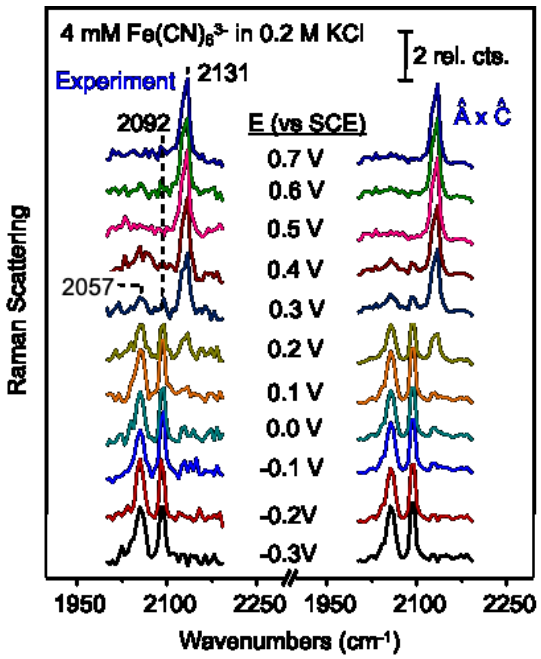

Figure 2. **Left:** Raman spectra recorded with the confocal probe volume positioned ~3 μm from the surface of an ITO-coated glass coverslip serving as the working electrode in a microscope stage mounted spectroelectrochemical cell. The cell was filled with 0.2 M KCl electrolyte containing 4 mM $K_3Fe(CN)_6$. Spectra were recorded with the working electrode poised at the indicated potentials. The acquisition time for each spectrum was 25 s, and the laser power at the sample was approximately 30 mW. **Right:** Spectra calculated from the product of the least-squares optimized pure spectral component matrix and concentration coefficient matrix.

3.2. *Modeling*. Least-squares regression analysis was applied to the spectral dataset in Figure 2 to develop a quantitative understanding of the potential-dependent response. This approach decomposes a matrix of spectral data (**D**) into a matrix of pure-component spectra (**A**) and a coefficient matrix (**C**) that defines the relative contribution of each pure component at a specific

state (e.g., equilibrium potential) of the system.[29-31] The relationship is given by the following equation: $\mathbf{D} = \mathbf{A} \times \mathbf{C}$. When the spectra in **D** are in columns, the pure-component spectra in **A** are also in columns and the elements of **C** ($c(i,j)$) specify the fractional contribution of the associated pure component (i) to the total response measured for the system in each state, j. Through a theoretical model of the chemical system, constraints can be applied to guide the least-squares optimization of the spectral vectors in **A** and coefficients in **C**.[29-31] However, in decomposing the potential-dependent spectra in Figure 2, only initial estimates of the pure-component spectral vectors in **A**, acquired at the ends of the applied potential range, were applied. No model constraints were otherwise imposed, in order to allow testing of a Nernstian model of the system response.

As a first step in the analysis of the experimental data in Figure 2, a **D** matrix composed of spectral intensities covering the region of the dominant bands (2000-2200 cm^{-1}) was prepared. A factor analysis[29] was performed on **D** and F-testing of the returned eigenvectors confirmed the presence of two potential-dependent components in the dataset. From knowledge of the chemical system under study, and inspection of the recorded spectra, one pure component is expected to be linked to ferricyanide and the other to ferrocyanide formed in the reduction reaction.

With the columns in **A** fixed at two, **A** was initialized using the first spectrum (0.7 V) and last spectrum (0.3 V) in **D** as approximate pure-component spectra, and a least-squares estimate of **C** ($\hat{\mathbf{C}}$) was obtained as follows:

$$\hat{\mathbf{C}} = [\mathbf{A}^{\mathbf{T}} \mathbf{A}]^{-1} \mathbf{A}^{\mathbf{T}} \mathbf{D}. \quad (1)$$

The elements in $\hat{\mathbf{C}}$ were then compared to expectations based on the Nernst equation. Assuming ferrocyanide and ferricyanide complexes are in the following equilibrium at the electrode-solution

interface: $Fe(CN)_6^{3-} + e- \rightleftharpoons Fe(CN)_6^{4}$, the surface concentrations of the redox species will be governed by:

$$\frac{C_R}{C_O} = 10^{-f'(E-E^{o\prime})} \quad (2)$$

In Eq 2, $f' = 2.303F/RT$, where F is the Faraday constant, R the universal gas constant and T the absolute temperature, $E^{o\prime}$ is the formal potential, E is the applied potential and C_O and C_R are the concentrations of $Fe(CN)_6^{3-}$ and $Fe(CN)_6^{4-}$, respectively, at the electrode surface. Applying the constraint $C_O + C_R = C_O^*$, where C_O^* is the bulk solution concentration of $Fe(CN)_6^{3-}$ (4.0 mM), Eq 2 can be rearranged in terms of the surface $Fe(CN)_6^{4-}$ mole fraction:

$$\frac{C_R}{C^*} = \left[10^{f'(E-E^{o\prime})} + 1\right]^{-1}, \quad (3)$$

or the surface $Fe(CN)_6^{3-}$ mol fraction:

$$\frac{C_O}{C^*} = \left[10^{-f'(E-E^{o\prime})} + 1\right]^{-1}. \quad (4)$$

The Nernstian relationships in Equations 3 and 4 map to the $c(i, j)$, which represent the mole fraction of species i ($Fe(CN)_6^{3-}$ or $Fe(CN)_6^{4-}$) present at the electrode surface at potential $E(j)$.

The initial $\hat{\mathbf{C}}$ values derived according to Equation 1 were plotted to confirm consistency with Equations 3 and 4. Then, with the $C_O + C_R = C_O^*$ constraint applied, the $c(i, j)$ were refined through use of the Matlab adapted Nelder-Mead simplex algorithm[37] to minimize the sum of the squares of the residuals, $\mathbf{R^T R}$, where:

$$\mathbf{R} = \mathbf{D} - \mathbf{A}\,\hat{\mathbf{C}}\,. \quad (5)$$

After convergence, vectors in $\mathbf{R}$ were inspected to ensure the residuals were random and reflected the expected noise in the spectral dataset. Pure-component spectra were calculated by least-squares projection of the coefficients back onto the data according to:

$$\hat{\mathbf{A}} = \mathbf{D}\,\hat{\mathbf{C}}^{\mathbf{T}}\,[\hat{\mathbf{C}}\;\;\hat{\mathbf{C}}^{\mathbf{T}}]^{-1}. \quad (6)$$

$\widehat{\mathbf{A}}$ was updated in each iteration of the refinement.

Figure 3A plots the optimized spectral vectors in $\widehat{\mathbf{A}}$ derived from the Figure 2 dataset. As anticipated, the vectors match the experimental Raman spectra of ferrocyanide and ferricyanide ions in an aqueous solution (Figure 3B). Similarly, the potential dependence of the refined $c(i,j)$ values (Figure 4) for each pure component is in accord with the Nernstian response (Equations 3 and 4) and the $E^{o\prime}$ and f' obtained are in excellent agreement with the values expected for the conditions of the experiments. While it would have been possible to derive best-fit values for $E^{o\prime}$ and f' using Equations 3 and 4 to constrain the least-squares optimization of the coefficients in $\mathbf{C}$,[30,31] instead only initial estimates of the vectors in $\mathbf{A}$ were made through the selection of spectra that are close to the expected pure components, enabling the $c(i,j)$ to be determined without assumptions on their potential dependence. The concentration vectors displayed in Figure 4 follow a trend consistent with the anticipated Nernstian response, yet they were obtained without reliance on Equations 3 and 4.

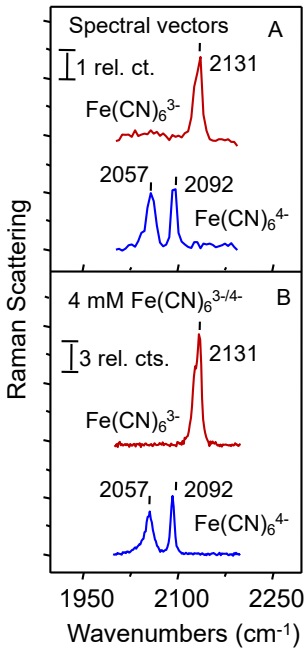

Figure 3. Least-squares optimized pure-component spectral vectors (A) and Raman spectra obtained from aqueous solutions containing 4 mM $K_3Fe(CN)_6$. and $K_4Fe(CN)_6$, as indicated (B).

The plotted data in Figure 4 also confirms the ability to determine analyte composition near the ITO film-solution interface quantitatively through confocal Raman microscopy measurements. The diffusion layer in the quiescent solution adjacent to the ITO film working electrode is predicted to extend a distance >100 μm from the film surface within the first few seconds of the 25 s spectral acquisition period.[38] With the confocal probe volume located approximately 3 μm above the ITO surface (Scheme 1), the $Fe(CN)_6^{3-}$ and $Fe(CN)_6^{4-}$ concentrations within the

femtoliter spatial region sampled should be representative of the ion concentrations at the ITO surface. For a diffraction-limited excitation beam focus, the confocal probe volume can be expected to have a diameter just smaller than the radiation wavelength (~λ/2 or ~0.4 μm at 660 nm) and an axial (*z*) dimension at 90 % detection efficiency of +/- 1.2 μm relative to the probe center.[19,20] The microscope immersion objective minimizes distortion from these probe volume dimensions by providing close refractive index matching to the sample.[39-41] Thus, the probe volume position and small size relative to the diffusion-layer thickness ensures spectra in Figure 2 reflect surface concentrations of the ions under study.

In Figure 2, the set of spectra on the right were calculated from the optimized $\hat{\mathbf{A}}$ and $\hat{\mathbf{C}}$ matrices. The noise reduction that accompanies least-squares refinement is evident along with improved ability to discriminate spectral features of $Fe(CN)_6^{3-}$ and $Fe(CN)_6^{4-}$ ions near the formal potential, where the equilibrium interfacial concentration of each is only ~2 mM. More generally, our ability to detect analyte at the millimolar level[25] and below in the reported work can be attributed to the confocal optical arrangement with its tight excitation beam focusing and high-efficiency collection of Raman scattered radiation.[22] Finally, although the cyclic voltammetry of ferricyanide at the ITO film electrode (Figure 1, middle) does not appear reversible at the moderate scan rate employed, the confocal Raman measurements that interrogate the near-surface region on a much

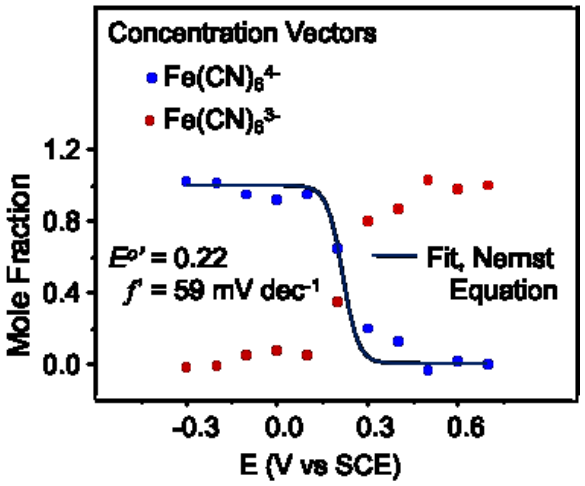

Figure 4. Optimized concentration vectors derived from least-squares modeling of the experimental spectral dataset in Figure 2. The solid line and $E^{o\prime}$ and f' quantities were obtained from non-linear least-squares fitting of the concentration vectors to Equation 3 ($Fe(CN)_6^{4-}$) and Equation 4 ($Fe(CN)_6^{3-}$). See text for details.

slower timescale are consistent with the expected reversibility of electrochemical transformations between ferricyanide and ferrocyanide.

3.3. *MV^{2+} reduction within Nafion*. With the ability to probe molecular composition[41,42] and transport[43] within polymer membranes and micron-scale particles, confocal Raman microscopy should be well suited to the study of polymer-modified electrodes for applications that include energy conversion, chemical synthesis, and sensing.[44] To test the strategy, the redox chemistry of MV^{2+} and transport of electrogenerated $MV^{+\bullet}$ within a Nafion phase was investigated. A 50-μm thickness membrane was first exchanged with MV^{2+} ions. After rinsing to remove excess MV^{2+}, the sample was laid over the central region of an ITO-coated coverslip mounted in the spectroelectrochemical cell. A porous glass frit was pressed to the membrane to hold it firmly against the ITO film surface. The cell was then filled with electrolyte solution and the potential was poised at -0.2 V, well above the formal potential for MV^{2+} reduction in the KCl electrolyte (ca. -0.7 V vs SCE).[45-48] Spectral data acquisition began after the confocal probe volume was positioned within the Nafion layer. A series of spectra recorded in 25-s intervals as the potential was stepped increasingly negative are displayed in Figure 5. A spectrum of Nafion in 0.2

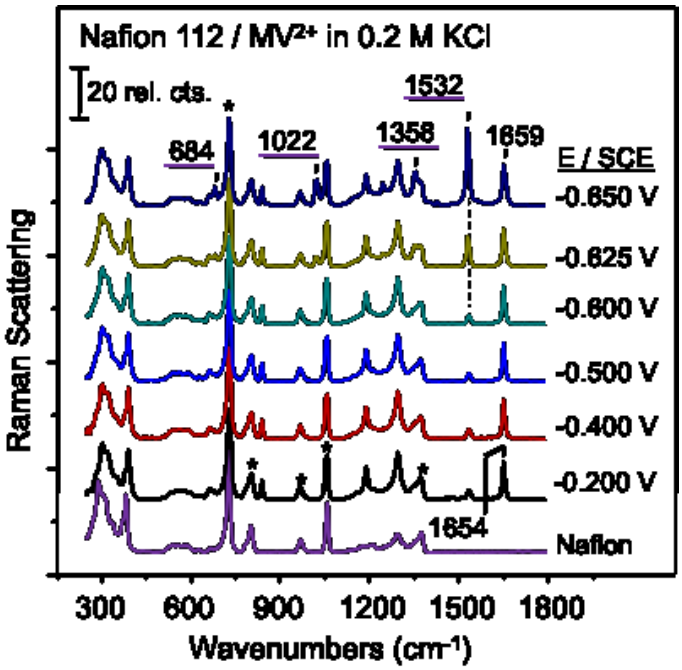

Figure 5. *In situ* Raman spectra recorded with the confocal probe volume positioned ~3 μm into the Nafion phase at the membrane / ITO film electrode interface. The Nafion was exchanged with MV^{2+} ions. Measurements were performed in 0.2 M KCl electrolyte solution. The acquisition time for each spectrum was 25 s, and the laser power at the sample was approximately 5 mW. Underlined peak positions indicate features assignable to $MV^{+\bullet}$ ions.

M KCl is included for reference. Star labels indicate Nafion peaks[49] that have no overlap with MV^{2+} or $MV^{+\bullet}$ bands. Between -0.2 V and -0.6 V, features other than Nafion are traceable to MV^{2+}.[46,47,50] Most notable among these are bands near 1654 cm^{-1} and (unlabeled) 1297 cm^{-1}, 1191 cm^{-1} and 970 cm^{-1}. In stepping to -0.625 V, growth in the peak at 1532 cm^{-1} and shifting of the 1654 cm^{-1} band to 1659 cm^{-1} signals the presence of $MV^{+\bullet}$. For excitation at 660 nm, the $MV^{+\bullet}$ features are resonantly enhanced enabling traces of the reduction product to be easily detected well below the formal potential for the MV^{2+} + e- $\rightleftharpoons$ $MV^{+\bullet}$ transformation.[46] Increasing the potential negative to -0.65 V, the 1532 cm^{-1} band continues to grow and additional $MV^{+\bullet}$ bands become evident across the 600 cm^{-1} - 1600 cm^{-1} region.

Figure 6 shows the dominant features for MV^{2+} and $MV^{+\bullet}$ at 1654 cm^{-1} and 1532 cm^{-1}, respectively, as they evolve over time following a step to -0.65 V. Spectra collected at less negative potentials (-0.60 V and -0.62 V) just prior to reaching -0.65 V are consistent with the presence of MV^{2+} within the confocal probe volume. Transitioning from -0.62 V to -0.65 V leads to a slight increase in intensity at 1532 cm^{-1} after 60 s. The band continues to grow steadily as spectra are collected on 60 s-intervals with the potential fixed at -0.65 V. During this period, the change in peak intensity at 1532 cm^{-1} is attributable to $MV^{+\bullet}$ species accumulation in the diffusion layer adjacent to the ITO film surface. Figure 7a depicts this change as a

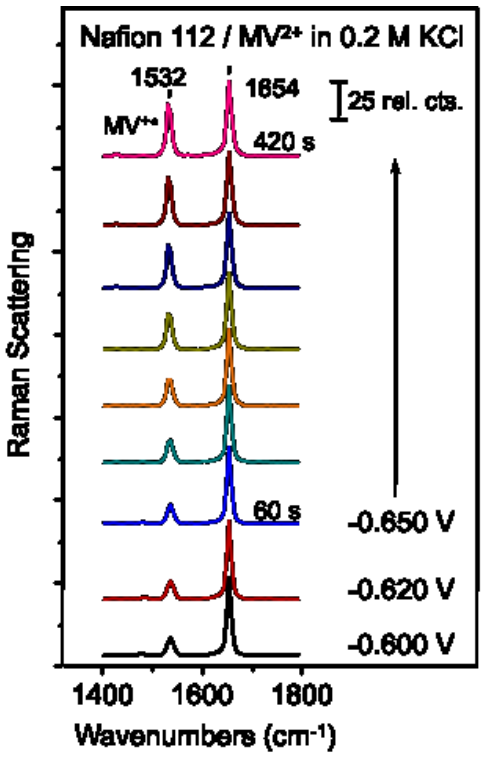

Figure 6. *In situ* Raman spectra that track $MV^{+\bullet}$ accumulation within the confocal probe volume as a function of time after the potential is stepped to -0.65 V. See text and Figure 5 legend for details.

function of the diffusion-layer thickness (δ) estimated from a simple one-dimensional model for $MV^{+\bullet}$ transport from the ITO surface through the adjacent bulk Nafion layer. The thickness was calculated from $\delta = \sqrt{2\,D\,t}$, where D is the diffusion coefficient for $MV^{+\bullet}$ in Nafion and t is the time following the step to the reaction potential. D was derived from recently reported studies of MV^{2+} and $MV^{+\bullet}$ diffusion within Nafion thin films prepared by casting onto carbon electrodes.[48] Assuming a diffusion coefficient for $MV^{+\bullet}$ of ~3 x 10^{-10} cm^2/s in the Nafion membrane,[48] the diffusion-layer thicknesses predicted are consistent with the expected axial confocal probe volume dimensions (≥ 2.4 μm) (Figure 7a). A probe with its center positioned 3 μm from the ITO surface, as anticipated in this case, can be expected to begin sensing $MV^{+\bullet}$ as the diffusional front advances toward a point 2 μm from the ITO surface.[20,41]

The initially slow change in 1532 cm^{-1} peak intensity (ΔI_{1532}) after stepping to -0.65 V in Figure 7a likely results at least in part from the presence of dissolved O_2 in the electrolyte, since it was not possible to maintain an inert atmosphere over the solution in these initial tests of the spectroelectrochemical cell. H_2O_2 produced from O_2 reduction is able to oxidize $MV^{+\bullet}$ and lower its concentration until an O_2 depletion layer develops in the near-surface region. The effect is evident in the plot of optical response versus $t^{-1/2}$ in Figure 7b. The signal from $MV^{+\bullet}$ ions becomes consistent with diffusional motion at long times, but $MV^{+\bullet}$ accumulation is slow early in the experiment.

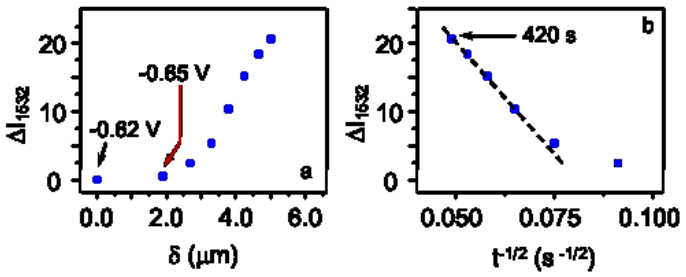

Figure 7. From spectra in Figure 6 recorded at -0.65 V showing the change in Raman scattering intensity at 1532 cm^{-1} plotted as a function of (a) the estimated diffusion-layer thickness and (b) $t^{-1/2}$.

The trend in Figure 7a also is affected by variation in detection efficiency across the axial dimension of the probe volume.[19,20,40,41]. The impact of this variation on spatial resolution in the measurement of analyte front advancement is under study. Strategies for determining the instrument response function[20,40] are being adapted to enable corrections and improved estimates of mass transport coefficients from spectral datasets that track analyte movement through the confocal probe volume.

Comparing spectra in Figures 5 and 6, differences in the potential dependence of MV^{2+} and $MV^{+\bullet}$ signals are evident. Sensitivity to probe volume positioning along the *z*-dimension is an important factor affecting responses in addition to the potential for O_2 interferences under conditions of the experiments. The preliminary measurements demonstrate the ability to adapt confocal Raman microscopy for the detection of electrogenerated redox species within ionic polymer materials and encourage further studies toward quantitation of mass transport within these films.

4. Conclusions

Confocal Raman microscopy offers unique capabilities for the study of electrogenerated redox species and transformations within electrode-supported films.[16] The reported work demonstrates the ability to measure molecular composition to within a few micrometers of the electrode surface and to follow the transport of an electrogenerated product within an ionic polymer matrix in contact with the electrode. For the case of a reversible redox couple at an ITO film / solution interface, least-squares regression analysis applied to spectral datasets confirmed adherence of the system to the expected Nernstian model. More generally, it is possible to adapt least squares[30,31] and other[29,43] types of modeling approaches in a similar manner to derive important physical parameters and associate values to spatial locations relative to the electrode surface plane as well as in-plane (*x*

and *y*) locations on the electrode. Finally, with sensitivity toward a wide range of molecular species, the confocal Raman microscopy spectroelectrochemical technique is applicable to the study of solvent and electrolyte properties under reaction conditions and changes coupled to redox processes.

Acknowledgments

We are grateful for support from the U.S. National Science Foundation through grants CBET-1922956 (CK), CBET-1921075 (SDM), and CHE-1904424 (JMH) and from the U.S. Department of Energy through Award DE-FG03-93ER14333 (JMH). CK also is thankful for support from the Texas Tech University faculty development leave program.

References

1. Farias, M. J.; Cheuquepan, W.; Tanaka, A. A.; Feliu, J. M. Unraveling the nature of active sites in ethanol electro-oxidation by site-specific marking of a Pt catalyst with isotope-labeled ^{13}CO *J. Phys. Chem. Lett.* **2018**, *9*, 1206-1210.
2. Farias, M. J. S.; Cheuquepan, W.; Tanaka, A. A.; Feliu, J. M. Identity of the most and least active sites for activation of the pathways for CO_2 formation from the electro-oxidation of methanol and ethanol on platinum *ACS Catal.* **2020**, *10*, 543-555.
3. Dong, J.-C.; Su, M.; Briega-Martos, V.; Li, L.; Le, J.-B.; Radjenovic, P.; Zhou, X.-S.; Feliu, J. M.; Tian, Z.-Q.; Li, J.-F. Direct *in situ* Raman spectroscopic evidence of oxygen reduction reaction intermediates at high-index Pt(*hkl*) surfaces *J. Am. Chem. Soc.* **2020**, *142*, 715-719.
4. Dong, J.-C.; Zhang, X.-G.; Briega-Martos, V.; Jin, X.; Yang, J.; Chen, S.; Yang, Z.-L.; Wu, D.-Y.; Feliu, J. M.; Williams, C. T.; Tian, Z.-Q.; Li, J.-F. *In situ* Raman spectroscopic evidence for oxygen reduction reaction intermediates at platinum single-crystal surfaces *Nat. Energy* **2019**, *4*, 60-67.
5. Wang, Y.-H.; Wei, J.; Radjenovic, P.; Tian, Z.-Q.; Li, J.-F. In situ analysis of surface catalytic reactions using shell-isolated nanoparticle-enhanced Raman spectroscopy *Anal. Chem.* **2019**, *91*, 1675-1685.

6. Watts, K. E.; Blackburn, T. J.; Pemberton, J. E. Optical spectroscopy of surfaces, interfaces, and thin films: A status report *Anal. Chem.* **2019**, *91*, 4235-4265.
7. *Diffraction and Spectroscopic Methods in Electrochemistry*; Alkire, R.; Kolb, D. M.; Lipkowski, J.; Ross, P. N., Eds.; Wiley-VCH: Weinheim, 2006; Vol. 9.
8. Korzeniewski, C.; Climent, V.; Feliu, J. M., Electrochemistry at Platinum Single Crystal Electrodes In *Electroanalytical Chemistry*; Zoski, C. and Bard, A. J., Eds.; Taylor & Francis: New York, 2012, pp 75-169.
9. Porter, M. D. IR External Reflection Spectroscopy: A Probe for Chemically Modified Surfaces *Anal. Chem.* **1988**, *60*, 1143A-1155A.
10. Kollath, V. O.; Liang, Y.; Mayer, F. D.; Ma, X.; Korzeniewski, C.; Karan, K. Model-based analyses of confined polymer electrolyte nanothin films experimentally probed by polarized ATR−FTIR spectroscopy *J. Phys. Chem. C* **2018**, *122*, 9578−9585.
11. Haynes, C. L.; McFarland, A. D.; Van Duyne, R. P. Surface-enhanced Raman spectroscopy *Anal. Chem.* **2005**, *77*, 338A-346A.
12. Deabate, S.; Huguet, P.; Morin, A.; Gebel, G.; Lanteri, Y.; Peng, Z.; Sutor, A. K. Raman microspectroscopy as a useful tool for in situ and operando studies of water transport in perfluorosulfonic membranes for PEMFCs *Fuel Cells* **2014**, *14*, 677-693.
13. Peng, Z.; Huguet, P.; Deabate, S.; Morin, A.; Sutor, A. K. Depth-resolved micro-Raman spectroscopy of tri-layer PFSA membrane for PEM fuel cells: how to obtain reliable inner water contents *J. Raman Spectrosc.* **2013**, *44*, 321-328.
14. Kendrick, I.; Fore, J.; Doan, J.; Loupe, N.; Vong, A.; Dimakis, N.; Diem, M.; Smotkin, E. S. Operando Raman micro-spectroscopy of polymer electrolyte fuel cells *J. Electrochem. Soc.* **2016**, *163*, H3152-H3159.
15. Loupe, N.; Doan, J.; Cruse, R.; DiMarzio, C. A.; Smotkin, E. S. Laser focal point sequestration for Raman micro-spectroscopy of thermally sensitive fuel cell catalytic layers *Electrochim. Acta* **2018**, *283*, 1079-1086.
16. Steimecke, M.; Seiffargh, G.; Bron, M. In situ characterization of Ni and Ni/Fe thin film electrodes for oxygen evolution in alkaline media by a Raman-coupled scanning electrochemical microscope setup *Anal. Chem.* **2017**, *89*, 10679-10686.
17. Gossage, Z. T.; Schorr, N. B.; Hernandez-Burgos, K.; Hui, J.; Simpson, B. H.; Montoto, E. C.; Rodriguez-Lopez, J. Interrogating charge storage on redox active colloids via combined

Raman spectroscoy and scanning electrochemical microscopy *Langmuir* **2017**, *33*, 9455-9463.

18. Schorr, N. B.; Jiang, A. G.; Rodrizuez-Lopez, J. Probing graphene interfacial reactivity via simultaneous and colocalized Raman-scanning electrochemical microscopy imaging and interrogation *Anal. Chem.* **2018**, *90*, 7848-7854.
19. Bridges, T.; Houlne, M.; Harris, J. M. Spatially resolved analysis of small particles by confocal Raman microscopy: Depth profiling and optical trapping *Anal. Chem.* **2004**, *76*, 576-584.
20. Korzeniewski, C.; Kitt, J. P.; Bukola, S.; Creager, S. E.; Minteer, S. D.; Harris, J. M. Single layer graphene for estimation of axial spatial resolution in confocal Raman microscopy depth profiling *Anal. Chem.* **2019**, *91*, 1049-1055.
21. Peterson, E. M.; Harris, J. M. Single-molecule fluorescence imaging of DNA at a potential-controlled interface *Langmuir* **2013**, *29*, 8292-8301.
22. Kitt, J. P.; Bryce, D. A.; Harris, J. M. Spatial filtering of a diode laser beam for confocal Raman microscopy *Appl. Spectrosc.* **2015**, *69*, 513-517.
23. Kitt, J. P.; Harris, J. M. Confocal Raman microscopy for in situ measurement of octanol-water partitioning within pores of individual C_{18}-functionalized chromatographic particles *Anal. Chem.* **2015**, *87*, 5340-5347.
24. Williams, K. P. J.; Pitt, G. D.; Batchelder, D. N.; Kip, B. J. Confocal Raman microspectroscopy using a stigmatic spectrograph and CCD detector *Appl. Spectrosc.* **1994**, *48*, 232-235.
25. Wang, Y.; McCreery, R. L. Evaluation of a diode laser/charge coupled device spectrometer for near-infrared Raman spectroscopy *Anal. Chem.* **1989**, *61*, 2647-2651.
26. Fryling, M. A.; Frank, C. J.; McCreery, R. L. Intensity calibration and sensitivity comparisons for CCD/Raman spectrometers *Appl. Spectrosc.* **1993**, *47*, 1965-1974.
27. Choquette, S. J.; Etz, E. S.; Hurst, W. S.; Blackburn, D. H.; Leigh, S. D. Relative intensity correction of Raman spectrometers: NIST SRMs 2241 through 2243 for 785 nm, 532 nm, and 488 nm/514.5 nm excitation *Appl. Spectrosc.* **2007**, *61*, 117-129.
28. Brandt, N. N.; Orovko, O. O.; Chikishev, A. Y.; Paraschuk, O. D. Optimization of the rolling-circle filter for Raman background subtraction *Appl. Spectrosc.* **2006**, *60*, 288-293.
29. Malinowski, E. R. *Factor Analysis in Chemistry*; 3rd ed.; Wiley: New York, 2002.

30. Rivera, D.; Peterson, P. E.; Uibel, R. H.; Harris, J. M. In situ adsorption studies at silica/solution interfaces by attenuated total internal reflection Fourier transform infrared spectroscopy: Examination of adsorption models in normal-phase liquid chromatography *Anal. Chem.* **2000**, *72*, 1543-1554.
31. Korzeniewski, C.; Adams, E.; Liu, D. Responses of hydrophobic and hydrophilic groups in Nafion differentiated by least squares modeling of infrared spectra recorded during thin film hydration *Appl. Spectrosc.* **2008**, *62*, 634-639.
32. Shi, Y.; Slaterbeck, A. F.; Seliskar, C. J.; Heineman, W. R. Spectroelectrochemical sensing based on multimode selectivity simultaneously achievable in a single device. 1. Demonstration of concept with ferricyanide *Anal. Chem.* **1997**, *69*, 3679-3686.
33. Ibanez, D.; Garoz-Ruiz, J.; Heras, A.; Colina, A. Simultaneous UV-visible absorption and Raman spectroelectrochemistry *Anal. Chem.* **2016**, *88*, 8210-8217.
34. van den Beld, W. T. E.; Odijk, M.; Vervuurt, R. H. J.; Weber, J.-W.; Bol, A. A.; van den Berg, A.; Eijkel, J. C. T. In-situ Raman spectroscopy to elucidate the influence of adsorption in graphene electrochemistry *Sci. Rep.* **2017**, *7*, 45080.
35. Nakagawa, I.; Shimanouchi, T. Infrared spectroscopic study on the co-ordination bond - II Infrared spectra of octahedral metal cyanide complexes *Spectrochim. Acta* **1962**, *18*, 101-113.
36. Nakamoto, K. *Infrared and Raman Spectra of Inorganic and Coordination Compounds*; Wiley: New York, 2009; Vol. 6th Edition.
37. Lagarias, J. C.; Reeds, J. A.; Wright, M. H.; Wright, P. E. Convergence properties of the Nelder-Mead simplex method in low dimensions *SIAM Journal of Optimization* **1998**, *9*, 112-147.
38. Bard, A. J.; Faulkner, L. R. *Electrochemical Methods: Fundamentals and Applications*; 2nd Ed.; Wiley: New York, 2001.
39. Froud, C. A.; Hayward, I. P.; Laven, J. Advances in the Raman depth profiling of polymer laminates *Appl. Spectrosc.* **2003**, *57*, 1468-1474.
40. de Grauw, C. J.; Sijtsema, N. M.; Otto, C.; Greve, J. Axial resolution of confocal Raman microscopes: Gaussian beam theory and practice *J. Microscopy* **1997**, *188*, 273-279.
41. Everall, N. J. Confocal Raman microscopy: Common errors and artefacts *Analyst* **2010**, *135*, 2512-2522.

42. Cai, R.; Abdellaoui, S.; Kitt, J. P.; Irvine, C.; Harris, J. M.; Minteer, S. D.; Korzeniewski, C. Confocal Raman microscopy for the determination of protein and quaternary ammonium ion loadings in biocatalytic membranes for electrochemical energy conversion and storage *Anal. Chem.* **2017**, *89*, 13290-13298.
43. Bridges, T. E.; Uibel, R. H.; Harris, J. M. Measuring diffusion of molecules into individual polymer particles by confocal Raman microscopy *Anal. Chem.* **2006**, *78*, 2121-2129.
44. Chen, H.; Simoska, O.; Lim, K.; Grattieri, M.; Yuan, M.; Dong, F.; Lee, Y. S.; Beaver, K.; Weliwatte, S.; Gaffney, E. M.; Minteer, S. D. Fundamentals, applications, and future directions of bioelectrocatalysis *Chem. Rev.* **2020**, *120*, 12903-12993.
45. Watanabe, T.; Honda, K. Measurement of the extinction coefficient of the methyl viologen cation radical and the efficiency of its formation by semiconductor photocatalysis *J. Phys. Chem.* **1982**, *86*, 2617-2119.
46. Forster, M.; Girling, R. B.; Hester, R. E. Infrared, Raman and resonance Raman investigations of methylviologen and its radical cation *J. Raman Spectrosc.* **1982**, *12*, 36-48.
47. Lu, T.; Birke, R. L.; Lombardi, J. R. Surface Raman spectroscopy of the three redox forms of methylviologen *Langmuir* **1986**, *2*, 305-309.
48. Chen, L.; Lin, C.; Compton, R. G. Electrochemical characterisation and comparison of transport in Nafion films and particles *Phys. Chem. Chem. Phys.* **2019**, *21*, 607-616.
49. Gruger, A.; Regis, A.; Schmatko, T.; Colomban, P. Nanostructure of Nafion membranes at different states of hydration - An IR and Raman study *Vib. Spectrosc.* **2001**, *26*, 215-225.
50. Dutta, P. K.; Incavo, J. A. Photoelectron transfer from tris(2,2'-bipyridine)ruthenium(II) to methylviologen in zeolite cages: A resonance Raman spectroscopic study *J. Phys. Chem.* **1987**, *91*, 4443-4446.